The Astrophysical Journal, 746:89 (8pp), 2012 February 10 doi:10.1088/0004-637X/746/1/89


# THE DARK MATTER DENSITY PROFILE OF THE FORNAX DWARF

John R. Jardel and Karl Gebhardt
Department of Astronomy, University of Texas at Austin, 1 University Station C1400, Austin, TX 78712, USA;
jardel@astro.as.utexas.edu, gebhardt@astro.as.utexas.edu
*Received 2011 August 10; accepted 2011 November 29; published 2012 January 27*

## ABSTRACT

We construct axisymmetric Schwarzschild models to measure the mass profile of the Local Group dwarf galaxy Fornax. These models require no assumptions to be made about the orbital anisotropy of the stars, as is the case for commonly used Jeans models. We test a variety of parameterizations of dark matter density profiles and find cored models with uniform density $\rho_c = (1.6 \pm 0.1) \times 10^{-2}\, M_\odot\, \mathrm{pc}^{-3}$ fit significantly better than the cuspy halos predicted by cold dark matter simulations. We also construct models with an intermediate-mass black hole, but are unable to make a detection. We place a $1\sigma$ upper limit on the mass of a potential intermediate-mass black hole at $M_\bullet \leqslant 3.2 \times 10^4\, M_\odot$.

*Key words:* dark matter – galaxies: dwarf – galaxies: individual (Fornax) – galaxies: kinematics and dynamics – Local Group

*Online-only material:* color figures

## 1. INTRODUCTION

Low-mass galaxies provide a unique testing ground for predictions of the cold dark matter (CDM) paradigm for structure formation, since they generally have a lower fraction of baryons than massive galaxies. These galaxies allow for a more direct measurement of the underlying dark matter potential, as the complicated effects of baryons on the dark matter are less pronounced. A particularly testable prediction of CDM is that all galaxies share a universal dark matter density profile, characterized by a cuspy inner power law $\rho \propto r^{-\alpha}$, where $\alpha = 1$ (Navarro et al. 1996b, hereafter NFW). Many authors have investigated low-mass spirals and found, in contrast to the predictions of CDM, dark matter density profiles with a flat inner core of slope $\alpha = 0$ (Burkert 1995; Persic et al. 1996; de Blok et al. 2001; Blais-Ouellette et al. 2001; Simon et al. 2005). This has launched the debate known as the core/cusp controversy.

A number of other studies have investigated the mass content of dwarf spheroidal galaxies (dSphs). Gilmore et al. (2007) give a comprehensive review of recent attempts to constrain the inner slope of their dark matter profiles with Jeans modeling (Jeans 1919; Binney & Tremaine 1987, chap. 4). When significant, cored profiles are preferred for all dSphs modeled (Gilmore et al. 2007, and references therein).

These results, however, are subject to a major caveat of Jeans modeling: it is complicated by the effect of stellar velocity anisotropy. Models fit to the line-of-sight component of the velocity dispersion, but anisotropy can severely affect the modeling of enclosed mass. Therefore, additional assumptions must be made. The studies presented in Gilmore et al. (2007) assume spherical symmetry and isotropy. Evans et al. (2009) show that a weakness of Jeans modeling is that given these assumptions combined with the cored light profiles observed in dSphs, the Jeans equations do not allow solutions with anything other than a cored dark matter profile.

Walker et al. (2009b) construct more sophisticated models and attempt to parameterize and fit for the anisotropy. As a result, preference for cored profiles becomes model dependent. They therefore are unable to put significant constraints on the slope of the dark matter profile. This highlights the main problem with Jeans modeling—it is highly dependent on the assumptions made.

Distribution function models are more general than Jeans models, and progress has been made applying them to a number of dSph systems (Kleyna et al. 2002; Wu 2007; Amorisco & Evans 2011). Nevertheless, these models still make strong assumptions such as spherical symmetry or isotropy, and models that do fit for anisotropy do so without using the information about the stellar orbits contained in the line-of-sight velocity distributions (LOSVDs).

We employ a fundamentally different modeling technique, known as Schwarzschild modeling, that allows us to use this information to self-consistently calculate both the enclosed mass and orbital anisotropy. Schwarzschild modeling is a mature industry, but one that has seldom been applied to the study of dSph galaxies (see Valluri et al. 2005).

In addition to being well suited for measuring dark matter profiles, Schwarzschild modeling has often been used to search for black holes at the centers of galaxies. Another unresolved issue relevant to the study of dSphs is whether they host an intermediate-mass black hole (IMBH). In a hierarchical merging scenario, smaller galaxies are thought to be the building blocks of larger galaxies. It is thought that all massive galaxies host a supermassive black hole (SMBH) at their center; therefore it is logical to believe that their building blocks host smaller IMBHs. Evidence for these IMBHs is scarce, however, and dynamical detections are even scarcer. The closest and lowest mass example of a dynamical measurement is an upper limit on the Local Group dSph NGC 205 of $M_\bullet \leqslant 2.2 \times 10^4\, M_\odot$ (Valluri et al. 2005). Black holes in this mass range can provide constraints on theories of black hole growth and formation. The two most prominent competing theories of nuclear black hole formation are direct collapse of primordial gas (Umemura et al. 1993; Eisenstein & Loeb 1995; Begelman et al. 2006) or accretion onto and mergers of seed black holes resulting from the collapse of the first stars (Volonteri & Perna 2005).

In this paper, we present axisymmetric, three-integral Schwarzschild models in an effort to determine the inner slope of the dark matter density profile as well as the orbit structure of the Fornax dSph. We also investigate the possibility of a central

IMBH. We assume a distance of 135 kpc to Fornax (Bersier 2000).

## 2. DATA

To construct dynamical models, we require a stellar light profile as well as stellar kinematics in the form of LOSVDs. We use published data for both the photometry and kinematics, and describe the steps taken to convert these data into useful input for our models.

### 2.1. Stellar Density

To determine the stellar density, we use a number density profile from Coleman et al. (2005) extending to 4590″. We linearly extrapolate the profile out to 6000″—a physical radius of 3.9 kpc at our assumed distance. We also extrapolate the profile inward at constant density from 90″ to 1″.

To convert to a more familiar surface brightness profile we apply an arbitrary zero-point shift in log space, adjusting this number so that the integrated profile returns a luminosity consistent with the value listed in Mateo (1998). Adopting an ellipticity of $e = 0.3$ (Mateo 1998), we deproject under the assumption that surfaces of constant luminosity are coaxial spheroids (Gebhardt et al. 1996), and for an assumed inclination of $i = 90°$.

### 2.2. Stellar Kinematics

We derive LOSVDs from individual stellar velocities published in Walker et al. (2009a). The data contain heliocentric radial velocities and uncertainties with a membership probability for 2633 Fornax stars. Most of these are single-epoch observations; however some are multi-epoch. Stars that have more than one observation are averaged, weighted by their uncertainties. After making a cut in membership probability at 90%, we are left with 2244 stars. Although a significant number of stars observed may be in binary or multiple systems, simulations have shown that such systems are unlikely to affect measured dispersions (Hargreaves et al. 1996; Olszewski et al. 1996; Mateo 1998).

We adopt a position angle P.A. = 41° (Walker et al. 2006). We assume symmetry with respect to both the major and minor axes and fold the data along each axis. To preserve any possible rotation, we switch the sign of the velocity whenever a star is flipped about the minor axis.

The transverse motion of Fornax contributes a non-negligible line-of-sight velocity to stars, particularly those at large galactocentric radius. Using the equations in Appendix A of Walker et al. (2008), we correct for this effect. We adopt values for the proper motion of $(\mu_\alpha, \mu_\delta) = (47.6, -36.0)$ mas century$^{-1}$ (Piatek et al. 2007) and assume the heliocentric radial velocity of Fornax is 53.3 km s$^{-1}$ (Piatek et al. 2002).

We divide our meridional grid into 20 radial bins, equally spaced in approximately log $r$ from 1″ to 5000″. There are five angular bins spaced equally in sin $\theta$ over 90° from the major axis to the minor axis (Gebhardt et al. 2000; Siopis et al. 2009). From the positions of the folded stellar velocity data, we determine the best binning scheme so that each grid cell contains at least 25 stars from which to recover the LOSVD. Our first bin with enough stars to meet this criterion is centered at 47″and the last bin is centered at 2500″. We therefore have two-dimensional kinematics coverage over the radial range 47″–2500″ (30 pc–1.6 kpc). At small radii the number density of stars with velocity measurements is low; thus our central LOSVDs have higher uncertainty compared to those at larger radii.

Within each grid cell, we calculate the LOSVD from discrete stellar velocities by using an adaptive kernel density estimate adapted from Silverman (1986) and explained in Gebhardt et al. (1996). We estimate the 1$\sigma$ uncertainties in the LOSVDs through bootstrap resamplings of the data (Gebhardt et al. 1996; Gebhardt & Thomas 2009). The bootstrap generates a new sample from the data itself by randomly picking $N$ data points, where $N$ is the total number of stars in a given bin, allowing the same point to be chosen more than once. We then estimate the LOSVD from that realization and repeat the procedure 300 times. The 68% confidence band on the LOSVDs corresponds to the 68% range of the realizations. We compare the velocity dispersion as measured by the LOSVDs with the biweight scale (i.e., a robust estimate of the standard deviation; see Beers et al. 1990) of the individual velocities and note good agreement.

Figure 1 plots the LOSVDs of four bins. Rather than parameterizing these LOSVDs with Gauss–Hermite moments, our models instead fit directly to the LOSVDs to constrain the kinematics of the galaxy. However, we do fit Gauss–Hermite moments for plotting purposes only. These data are presented in Figure 2 for stars that have been grouped into bins near the major axis (blue) and minor axis (red). Near the center of the galaxy the density of stars with kinematics is sparse, so we therefore group stars into annular bins covering all angles (green). We estimate the 1$\sigma$ uncertainties of the Gauss–Hermite moments by fitting to each of the 300 realizations calculated during the bootstrap discussed above. The error bars plotted contain 68% of the 300 realizations.

## 3. DYNAMICAL MODELS

The modeling code we use is described in detail in Gebhardt et al. (2003), Thomas et al. (2004, 2005), and Siopis et al. (2009) and is based on the technique of orbit superposition (Schwarzschild 1979). Similar axisymmetric codes are described in Rix et al. (1997), van der Marel et al. (1998), Cretton et al. (1999), and Valluri et al. (2004), while van den Bosch et al. (2008) present a fully triaxial Schwarzschild code. Our code begins by choosing a trial potential that is a combination of the stellar density, dark matter density, and possibly a central black hole. We then launch ∼15,000 orbits carefully chosen to uniformly sample the isolating integrals of motion. In an axisymmetric potential, orbits are restricted by three isolating integrals of motion, $E$, $L_z$, and the non-classical "third integral" $I_3$. As it is not possible to calculate $I_3$ a priori, we use a carefully designed scheme to systematically sample $I_3$ for each pair of $E$ and $L_z$ (Thomas et al. 2004; Siopis et al. 2009). Orbits are integrated for many dynamical times and each orbit is given a weight $w_i$. We find the combination of $w_i$ that best reproduces the observed LOSVDs and light profile via a $\chi^2$ minimization subject to the constraint of maximum entropy (Siopis et al. 2009).

We run models by varying three parameters—the stellar $M/L_V$ and two parameters specifying the dark matter density profile. Some models are also run with a central black hole whose mass is varied in addition to the other three model parameters. Each model is assigned a value of $\chi^2$ and we identify the best-fitting model as that with the lowest $\chi^2$. We determine the 68% confidence range on parameters by identifying the

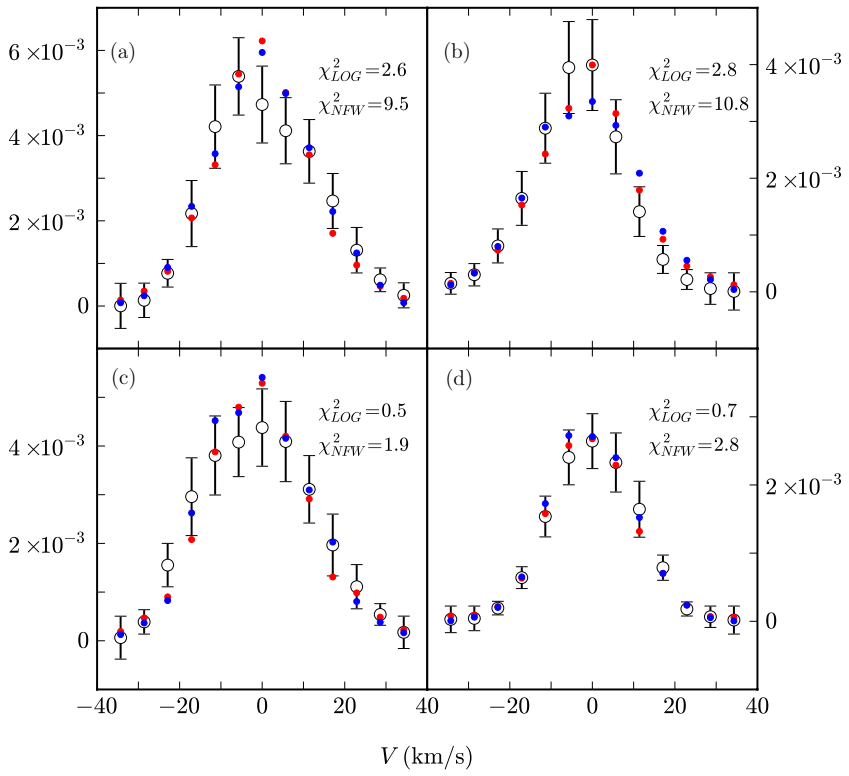


**Figure 1.** Line-of-sight velocity distributions of four bins. Open circles with error bars are the data. Overplotted are the model values for the best-fitting cored model (red) and NFW model (blue). Bins are located at (a) $R = 297''$, $\theta = 18°$; (b) $R = 550''$, $\theta = 18°$; (c) $R = 1008''$, $\theta = 45°$; and (d) $R = 2484''$, $\theta = 45°$. Quoted $\chi^2$ values are unreduced.

(A color version of this figure is available in the online journal.)

portion of their marginalized $\chi^2$ curves that lie within $\Delta\chi^2 = 1$ of the overall minimum.

### 3.1. Model Assumptions

Our trial potential is determined by solving Poisson's equation for an assumed trial density distribution. On our two-dimensional polar grid, this takes the form

$$\rho(r, \theta) = \frac{M}{L}\nu(r, \theta) + \rho_{\rm DM}(r), \quad (1)$$

where $M/L$ is the stellar mass-to-light ratio, assumed constant with radius, and $\nu(r, \theta)$ is the unprojected luminosity density. The assumed dark matter profile $\rho_{\rm DM}(r)$ is discussed below. For simplicity, we assume Fornax is edge-on in all our models.

### 3.2. Dark Matter Density Profiles

We parameterize the dark matter halo density with a number of spherical density profiles. We use NFW halos:

$$\rho_{\rm DM}(r) = \frac{200}{3}\frac{A(c)\rho_{\rm crit}}{(r/r_s)(1 + r/r_s)^2}, \quad (2)$$

where

$$A(c) = \frac{c^3}{\ln(1 + c) - c/(1 + c)}$$

and $\rho_{\rm crit}$ is the present critical density for a closed universe. The two parameters we fit for are the concentration $c$ and scale radius $r_s$. We also use halos derived from the logarithmic potential:

$$\rho_{\rm DM}(r) = \frac{V_c^2}{4\pi G}\frac{3r_c^2 + r^2}{\left(r_c^2 + r^2\right)^2}. \quad (3)$$

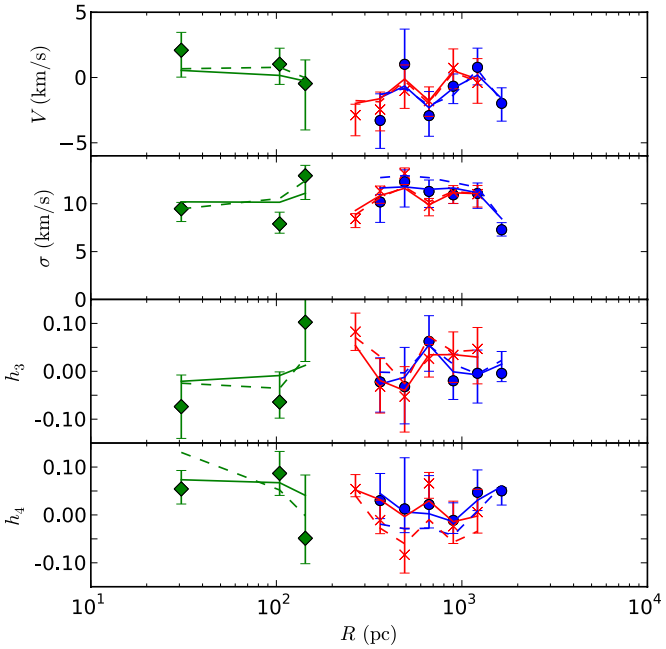


**Figure 2.** Gauss–Hermite moments for stars near the major axis (blue), minor axis (red), and averaged over all angles (green). Solid lines correspond to the best-fit model with a cored dark matter halo, dashed lines are for the best-fit model with an NFW halo.

(A color version of this figure is available in the online journal.)

These models feature a flat central core of density $\rho_c = 3V_c^2/4\pi G r_c^2$ for $r \lesssim r_c$ and an $r^{-2}$ profile for $r > r_c$. We fit for $V_c$ and $r_c$, the asymptotic circular speed at $r = \infty$ and

**Table 1**
Best-fit Model Parameters

| DM Profile | $\chi^2$ | $\frac{M}{L_V}$ | $c$ | $r_s$ (kpc) | $\rho_c$ ($M_\odot$ pc$^{-3}$) | $M_\bullet$ ($M_\odot$) | $N_{\rm model}$ |
|---|---|---|---|---|---|---|---|
| NFW | 239.8 | $1.3 \pm 0.6$ | $4.1 \pm 0.26$ | $11.7 \pm 1.4$ | ... | ... | 3124 |
| Log | 162.6 | $1.5 \pm 0.5$ | ... | ... | $1.6 \pm 0.1 \times 10^{-2}$ | ... | 4319 |
| Log | 162.6 | $1.6 \pm 0.2$ | ... | ... | $1.6 \pm 0.1 \times 10^{-2}$ | $\leqslant 3.2 \times 10^4$ | 3423 |

**Notes.** Best-fit parameters for NFW and cored logarithmic dark matter halos. $\chi^2$ is unreduced and the number of degrees of freedom is the same for each model. Model parameters and $1\sigma$ uncertainties are quoted. $N_{\rm model}$ lists the number of models that run for the corresponding parameterization.

core radius, respectively. We run over 10,000 models with only three distinct parameterizations: NFW halos, and logarithmic models with and without an IMBH.

## 4. RESULTS

We find significant evidence for cored logarithmic dark matter density profiles. These models are preferred at the $\Delta\chi^2 = 77$ level when compared to models with an NFW halo, a highly significant result. Perhaps more convincingly, the values for the concentration preferred by our models are around $c = 4$. Only relatively recently formed structures like galaxy clusters are expected to have concentrations this low (NFW).

Table 1 summarizes the results of our models, while Figures 1 and 2 illustrate the preference for cored models over models with an NFW halo in fitting to the kinematics. We stress again that LOSVDs like those plotted in Figure 1 are the kinematic constraints and not the Gauss–Hermite moments of Figure 2.

While we fit for $V_c$ and $r_c$ in the cored models, these parameters are strongly degenerate. Our model grid extends to 3.3 kpc; thus any model with $r_c > 3.3$ kpc has a uniform density $\rho_c = 3V_c^2/4\pi G r_c^2$ over the entire range of our model. Furthermore, we have no velocity information from stars past $R \geqslant 1.6$ kpc and therefore cannot constrain the kinematics in the outer parts of the galaxy. Thus, for models with $r_c \gtrsim 1.6$ kpc, $\rho_c$ is now the only parameter that differentiates between models. As $\rho_c$ is dependent on both $V_c$ and $r_c$, the latter two parameters are completely degenerate.

Figure 3 illustrates this effect. Plotted are the $\chi^2$ curves for each model parameter. Lines of the same color indicate a common parameterization of the mass profile (e.g., cored + IMBH). While the $\chi^2$ for both $V_c$ and $r_c$ asymptote to large values, $\rho_c$ is tightly constrained. Note that the behavior of $r_c$ for logarithmic profiles with an IMBH (green line) is a result of incomplete parameter sampling. With a more densely sampled parameter space, the $\chi^2$ curve for $r_c$ for cored models with an IMBH would likely asymptote to large $r_c$ in a similar fashion as models without an IMBH (red curve).

The addition of a central black hole to the mass profile does not make a noticeable difference to the overall $\chi^2$ for most values of $M_\bullet$. We therefore place a $1\sigma$ upper limit on $M_\bullet \leqslant 3.2 \times 10^4\, M_\odot$.

We plot the mass profile for our best-fit model in Figure 4 (solid black line with surrounding 68% confidence region). This is a cored logarithmic dark matter profile without a central black hole. The mass profile of our best-fit dark halo is plotted as the dashed line, and the stellar mass profile is plotted in red. The contribution of dark matter to the total mass increases with radius as the local dynamical mass-to-light ratio rises from approximately ~2 to greater than 100 in the outermost bin of our model.

### 4.1. Orbit Structure

We construct a distribution function for the galaxy from the set of orbital weights $w_i$ resulting from the $\chi^2$ minimization of our best-fit model. To explore the orbit structure, we determine the internal (unprojected) moments of the distribution function in spherical coordinates. Streaming motions in the $\mathbf{r}$ and $\boldsymbol{\theta}$ directions are assumed to be zero. In this coordinate system, cross terms of the velocity dispersion tensor are zero.

Figure 5 plots the anisotropy in the diagonal components of the dispersion tensor. While some panels show an average value near unity, there are regions in every panel where the ratio plotted is different from one. Additionally, we define the tangential velocity dispersion $\sigma_t \equiv \sqrt{(1/2)(\langle v_\phi^2\rangle + \sigma_\theta^2)}$, where $\langle v_\phi^2\rangle$ is the second moment $\langle v_\phi^2\rangle = \sigma_\phi^2 + V_\phi^2$ and $V_\phi^2$ is the mean rotation velocity. With this definition, we plot the ratio $\sigma_r/\sigma_t$ in the bottom panels of Figure 5 to investigate whether orbits are radially or tangentially biased. From these plots, it is clear that the common assumptions of Jeans modeling—constant or zero anisotropy—are unrealistic. We find that at most radii in the galaxy, orbits are radially biased. The uncertainty in the anisotropy is largest at small radii, as evidenced by the size of the 68% confidence regions in Figure 5. This is likely due to the sparsity of kinematics in the inner part of the galaxy (there are limits to how closely target fibers can be spaced in multi-fiber spectroscopy).

In a recent paper, Kazantzidis et al. (2011) simulated the effects of tidal stirring on a number of dSph progenitors around a Milky Way sized halo. They found radial anisotropy in all of the final remnants, and our models are consistent with these findings.

## 5. DISCUSSION

### 5.1. Cores and Cusps

Our analysis shows that for the Fornax dwarf an NFW dark matter halo with inner slope $\alpha = 1$ is rejected with high confidence. We have kinematics from 30 pc to 1.6 kpc, and over this range the models prefer an $\alpha = 0$ uniform density core with $\rho_c = 1.6 \times 10^{-2}\, M_\odot\, {\rm pc}^{-3}$. We do not attempt to fit for models with an intermediate value of the slope $0 \leqslant \alpha \leqslant 1$. Further investigation is necessary before we can conclude that the best-fitting dark matter profile is the logarithmic model. The steep $\alpha = 1$ cusp of the NFW profile is, however, robustly ruled out.

The models, in general, seem to prefer less mass in the areas over which we have kinematic constraints. In NFW models, the concentration $c$ sets the normalization (or $y$-intercept) of the density profile. Because $c$ cannot be lowered below an astrophysically reasonable limit, NFW models enclose more mass than cored models. This difference is reflected in the $\chi^2$

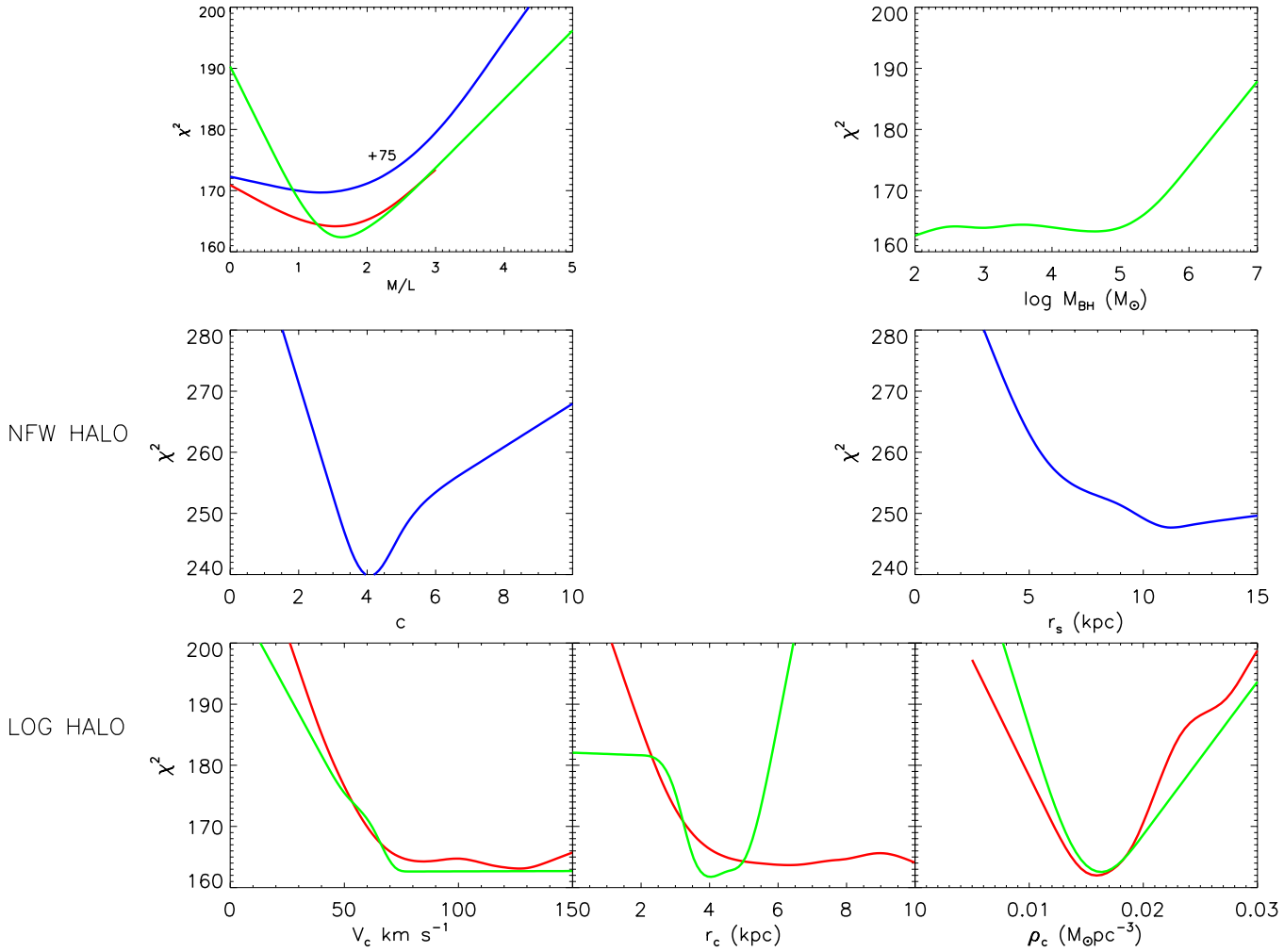


**Figure 3.** $\chi^2$ curves for all parameterizations of the mass profile. NFW halos (blue) are parameterized by concentration $c$ and scale radius $r_s$. Logarithmic halos with an IMBH (green) and without an IMBH (red) are specified by $V_c$ and $r_c$, respectively. We also plot core density $\rho_c = 3V_c^2/4\pi G r_c^2$ as it is the controlling parameter over the radial range of our models. We fit for stellar $M/L_V$ in all models (upper left panel). NFW models have much higher $\chi^2$ and are scaled down by 75 to fit on the same axis. Black hole mass for logarithmic halos with an IMBH (green) is plotted in the upper right panel. Note that the apparent minimum in $r_c$ for logarithmic halos with an IMBH is due to incomplete parameter sampling.

(A color version of this figure is available in the online journal.)

difference between cored and NFW models, as the kinematics are best fitted by models with less mass. Figure 2 hints at this as the best-fit NFW model (dashed line) typically has higher values for $\sigma$ than either the data or best-fitting cored model (solid line).

Several groups have approached the core/cusp issue in dSphs by taking advantage of the fact that some dSphs host multiple populations of tracer stars that are chemically and dynamically distinct. By fitting models to each component, the underlying dark matter profile can be modeled more accurately. Amorisco & Evans (2012) fit two-component distribution function models to Sculptor, while Walker & Peñarrubia (2011) apply a convenient mass estimator (discussed below) to each stellar component in Sculptor and Fornax. It is believed that this mass estimator is unaffected by orbital anisotropy; thus their method yields a robust determination of the dynamical mass at two locations in the galaxy—allowing for the slope of the dark matter profile to be measured. Each of these studies finds models with a cored dark matter halo preferable to the predicted cuspy NFW profile.

It must be noted, however, that we are not observing the pristine initial dark matter distribution in this galaxy. Rather, it has likely been modified by complex baryonic processes over the lifetime of the galaxy. These processes may include adiabatic compression (Blumenthal et al. 1986), halo rebounding following baryonic mass loss from supernovae (Navarro et al. 1996a), or possibly dynamical friction acting on clumps of baryons (El-Zant et al. 2001; but see also Jardel & Sellwood 2009). Although we chose this galaxy because these effects were likely to be small, they are nevertheless not well understood and our result must be taken in that context.

### 5.2. Central IMBH

We are unable to place a significant constraint on the mass of a central IMBH. Figure 3 (upper right) shows the marginalized $\chi^2$ curve against IMBH mass for cored dark matter density profiles. The curve asymptotes to low values of IMBH; thus we are only capable of placing an upper limit on the mass of any potential IMBH. Furthermore, our best-fit cored model with and without an IMBH has the same $\chi^2$. We therefore impose a $1\sigma$ upper limit on $M_\bullet \leqslant 3.2 \times 10^4\, M_\odot$. It is unfortunate that we are not able to place a lower limit on $M_\bullet$ because measurements of black holes in the range $M_\bullet \lesssim 10^4\, M_\odot$ place direct constraints on SMBH formation mechanisms (Van Wassenhove et al. 2010). Our models, however, do robustly rule out a black hole of larger mass.

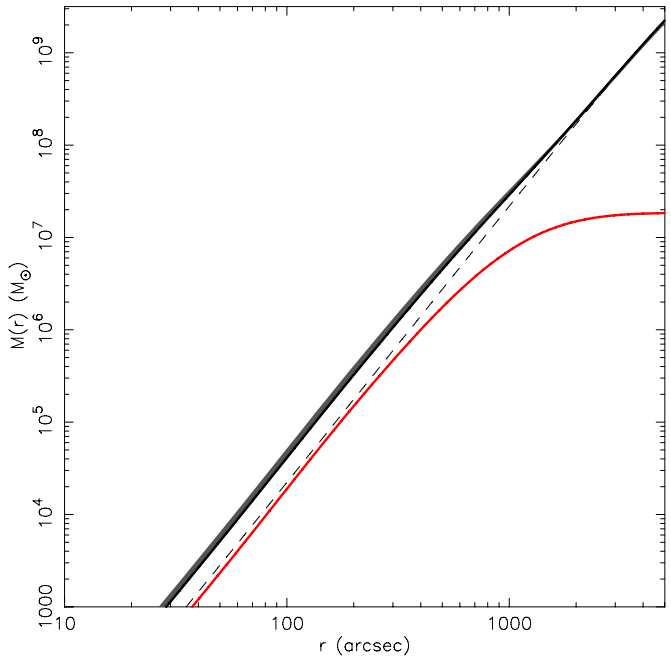


**Figure 4.** Total enclosed mass for our best-fit model (black line with surrounding confidence region). Red line is the enclosed stellar mass. Dashed line is our best-fit dark matter halo.

(A color version of this figure is available in the online journal.)

In massive galaxies it is thought that the radius of influence, $R_{\rm inf} \sim GM_\bullet/\sigma^2$, must be resolved in order to detect and precisely measure a black hole (Gebhardt et al. 2003; Kormendy 2004; Ferrarese & Ford 2005; Gültekin et al. 2009). Using our upper limit on $M_\bullet$ we can calculate the maximum radius of influence of a potential black hole. Estimating the central velocity dispersion at $\sigma \sim 10\,{\rm km\,s^{-1}}$ gives an upper limit for $R_{\rm inf} \lesssim 14$ pc. Our kinematics start at $R = 26$ pc, so it is not surprising that the minimum black hole mass we were able to detect has $R_{\rm inf}$ close to 26 pc. To detect smaller black holes, we require kinematics of stars closer to the center of the galaxy.

We are able to detect the dynamical influence of a black hole with a similar mass as Valluri et al. (2005) detect in NGC 205, but with kinematics of much lower resolution. Our innermost model bin is centered around 30 pc whereas they use high-resolution kinematics from the *Hubble Space Telescope* to resolve spatial scales less than 1 pc. The advantage we have is that the central velocity dispersion is much smaller in Fornax, which makes $R_{\rm inf}$ larger for fixed $M_\bullet$. NGC 205 is also more than five times as distant as Fornax.

### 5.3. Mass Estimators

Several authors have come up with convenient estimators of total mass within a given radius for Local Group dSphs. Strigari et al. (2008) use the mass enclosed within 300 pc, while Walker et al. (2009b) and Wolf et al. (2010) find a similar expression for the mass contained within the projected and unprojected half-light radii, respectively. These estimators bear striking resemblance to a result obtained by Cappellari et al. (2006) derived from integral field kinematics of massive elliptical galaxies, and they all hint at an easy way to determine dynamical masses without expensive modeling. They are believed to be insensitive to velocity anisotropy based on the derivation in Wolf

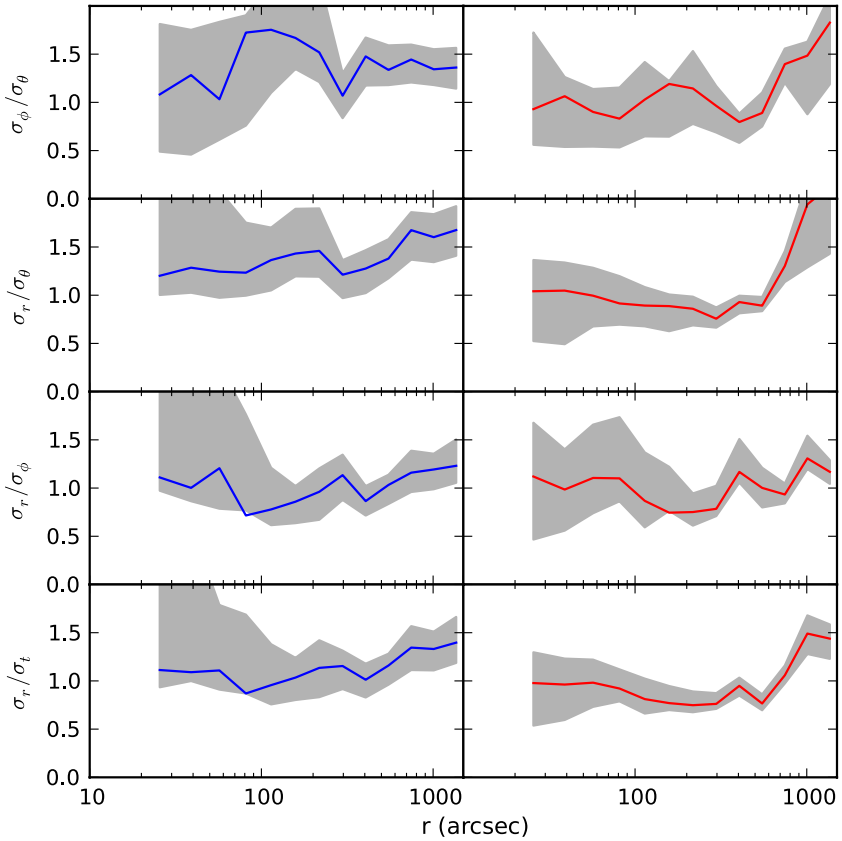


**Figure 5.** Anisotropy in various components of the velocity dispersion tensor. Shaded regions correspond to the 68% confidence regions; solid lines plot the best-fit model. Left- and right-hand panels plot stars near the major and minor axes, respectively.

(A color version of this figure is available in the online journal.)

et al. (2010), and we compare their estimates to our models as a check on this.

For the mass contained within 300 pc we measure $M_{300} = 3.5^{+0.77}_{-0.11} \times 10^6\ M_\odot$, roughly a factor of three smaller than Strigari et al. (2008) who measure $M_{300} = 1.14^{+0.09}_{-0.12} \times 10^7\ M_\odot$ using Jeans models with parameterized anisotropy.

The Cappellari et al. (2006), Walker et al. (2009b), and Wolf et al. (2010) mass estimators are all of the form

$$M(r_{\rm est}) = k \left\langle \sigma^2_{\rm LOS} \right\rangle R_e, \quad (4)$$

where $r_{\rm est}$ is the radius at which the estimator is valid. For Cappellari et al. (2006) and Walker et al. (2009b) $r_{\rm est} = R_e$ (the projected half-light radius), while for Wolf et al. (2010) $r_{\rm est} = r_e$ (the unprojected half-light radius). Other than the projected/unprojected difference, each estimator differs only by the value of the constant $k$. In order to more fairly compare between these estimators and our models, we use the values for the luminosity-weighted line-of-sight velocity dispersion $\langle \sigma^2_{\rm LOS} \rangle = 11.3^{+1.0}_{-1.8}\,{\rm km s^{-1}}$, projected half-light radius $R_e = 689$ pc, and unprojected half-light radius $r_e = 900$ pc that we calculate from the data used in our models.

Our best-fitting model has $M(R_e) = 3.9^{+0.46}_{-0.11} \times 10^7\ M_\odot$ and $M(r_e) = 5.8^{+1.0}_{-0.2} \times 10^7\ M_\odot$. With each group's value for $k$ and our kinematics, the mass estimates are $M(R_e) \approx 5.1^{+1.0}_{-1.5} \times 10^7\ M_\odot$ (Walker et al. 2009b), $M(r_e) \approx 8.1^{+1.6}_{-2.4} \times 10^7\ M_\odot$ (Wolf et al. 2010), and $M(R_e) \approx 1.0^{+0.3}_{-0.2} \times 10^8\ M_\odot$ (Cappellari et al. 2006). Our model is broadly consistent with both the Walker et al. (2009b) and Wolf et al. (2010) estimators.

The evidence that mass estimators are anisotropy independent comes largely from comparison to spherical Jeans models (except Cappellari et al. 2006). The weakness of these models is that the anisotropy must be parameterized and is restricted to be a function of radius only. Our models are not subject to these constraints since the anisotropy is calculated non-parametrically and is free to vary with position angle. We suggest that the best way to prove the accuracy of mass estimators is to compare with models that can self-consistently calculate both mass and anisotropy for realistic potentials.

For bright elliptical galaxies, Cappellari et al. (2006) and Thomas et al. (2011) have done just that. In these cases, the mass estimates are checked against masses derived from axisymmetric Schwarzschild modeling and good agreement is found. Ours is the first study to perform a similar test with dSphs, and there is no reason to assume that success with bright ellipticals guarantees accuracy in the dSph regime. The results from our comparison above are nevertheless reassuring.

### 5.4. Tidal Effects

The principle of orbit superposition, and hence our entire modeling procedure, relies on the assumption that the galaxy is bound and in a steady state. The amount of tidal stripping in Fornax due to the effect of its orbit through the Milky Way's halo is not well known. For reasonable values of Fornax total mass $m$, Milky Way mass $M$, and Galactocentric radius $R_0$, the tidal radius of Fornax is $r_t \sim (m/3M)^{1/3} R_0 \sim 13.5$ kpc. This estimate of $r_t$ is sufficiently larger than our model grid that we would not expect tidal effects to be important over the radial range of our models. If Fornax is on an eccentric orbit about the Milky Way, however, the above equation for $r_t$ is not valid and estimation of the tidal radius is not as straightforward. Fortunately, studies investigating its transverse motion suggest the orbit of Fornax is roughly circular (Piatek et al. 2007; Walker et al. 2008).

K.G. acknowledges support from NSF-0908639. We thank the Texas Advanced Computing Center (TACC) for providing state-of-the-art computing resources. We are grateful to the Magellan/MMFS Survey collaboration for making the stellar velocity data publicly available. Additionally, we thank Matthew Walker, Mario Mateo, Joe Wolf, and the anonymous referee for helpful comments on an earlier draft of the paper.

## REFERENCES

Amorisco, N. C., & Evans, N. W. 2012, MNRAS, 419, 184
Amorisco, N. C., & Evans, N. W. 2011, MNRAS, 411, 2118
Beers, T. C., Flynn, K., & Gebhardt, K. 1990, AJ, 100, 32
Begelman, M. C., Volonteri, M., & Rees, M. J. 2006, MNRAS, 370, 289
Bersier, D. 2000, ApJ, 543, L23
Binney, J., & Tremaine, S. 1987, Galactic Dynamics (Princeton, NJ: Princeton Univ. Press)
Blais-Ouellette, S., Amram, P., & Carignan, C. 2001, AJ, 121, 1952
Blumenthal, G. R., Faber, S. M., Flores, R., & Primack, J. R. 1986, ApJ, 301, 27
Burkert, A. 1995, ApJ, 447, L25
Cappellari, M., Bacon, R., Bureau, M., et al. 2006, MNRAS, 366, 1126
Coleman, M. G., Da Costa, G. S., Bland-Hawthorn, J., & Freeman, K. C. 2005, AJ, 129, 1443
Cretton, N., de Zeeuw, P. T., van der Marel, R. P., & Rix, H. 1999, ApJS, 124, 383
de Blok, W. J. G., McGaugh, S. S., Bosma, A., & Rubin, V. C. 2001, ApJ, 552, L23
Eisenstein, D. J., & Loeb, A. 1995, ApJ, 443, 11
El-Zant, A., Shlosman, I., & Hoffman, Y. 2001, ApJ, 560, 636
Evans, N. W., An, J., & Walker, M. G. 2009, MNRAS, 393, L50
Ferrarese, L., & Ford, H. 2005, Space Sci. Rev., 116, 523
Gebhardt, K., Bender, R., Bower, G., et al. 2000, ApJ, 539, L13
Gebhardt, K., Richstone, D., Ajhar, E. A., et al. 1996, AJ, 112, 105
Gebhardt, K., Richstone, D., Tremaine, S., et al. 2003, ApJ, 583, 92
Gebhardt, K., & Thomas, J. 2009, ApJ, 700, 1690
Gilmore, G., Wilkinson, M. I., Wyse, R. F. G., et al. 2007, ApJ, 663, 948
Gültekin, K., Richstone, D. O., Gebhardt, K., et al. 2009, ApJ, 698, 198
Hargreaves, J. C., Gilmore, G., & Annan, J. D. 1996, MNRAS, 279, 108
Jardel, J. R., & Sellwood, J. A. 2009, ApJ, 691, 1300
Jeans, J. H. 1919, Phil. Trans. R. Soc. A, 218, 157
Kazantzidis, S., Łokas, E. L., Callegari, S., Mayer, L., & Moustakas, L. A. 2011, ApJ, 726, 98
Kleyna, J., Wilkinson, M. I., Evans, N. W., Gilmore, G., & Frayn, C. 2002, MNRAS, 330, 792
Kormendy, J. 2004, in Coevolution of Black Holes and Galaxies, ed. L. C. Ho (Cambridge: Cambridge Univ. Press), 1
Mateo, M. L. 1998, ARA&A, 36, 435
Navarro, J. F., Eke, V. R., & Frenk, C. S. 1996a, MNRAS, 283, L72
Navarro, J. F., Frenk, C. S., & White, S. D. M. 1996b, ApJ, 462, 563
Olszewski, E. W., Pryor, C., & Armandroff, T. E. 1996, AJ, 111, 750
Persic, M., Salucci, P., & Stel, F. 1996, MNRAS, 281, 27
Piatek, S., Pryor, C., Bristow, P., et al. 2007, AJ, 133, 818
Piatek, S., Pryor, C., Olszewski, E. W., et al. 2002, AJ, 124, 3198
Rix, H., de Zeeuw, P. T., Cretton, N., van der Marel, R. P., & Carollo, C. M. 1997, ApJ, 488, 702
Schwarzschild, M. 1979, ApJ, 232, 236
Silverman, B. W. 1986, Density Estimation for Statistics and Data Analysis (London: Chapman and Hall)
Simon, J. D., Bolatto, A. D., Leroy, A., Blitz, L., & Gates, E. L. 2005, ApJ, 621, 757
Siopis, C., Gebhardt, K., Lauer, T. R., et al. 2009, ApJ, 693, 946
Strigari, L. E., Bullock, J. S., Kaplinghat, M., et al. 2008, Nature, 454, 1096
Thomas, J., Saglia, R. P., Bender, R., et al. 2004, MNRAS, 353, 391
Thomas, J., Saglia, R. P., Bender, R., et al. 2005, MNRAS, 360, 1355
Thomas, J., Saglia, R. P., Bender, R., et al. 2011, MNRAS, 415, 545
Umemura, M., Loeb, A., & Turner, E. L. 1993, ApJ, 419, 459
Valluri, M., Ferrarese, L., Merritt, D., & Joseph, C. L. 2005, ApJ, 628, 137
Valluri, M., Merritt, D., & Emsellem, E. 2004, ApJ, 602, 66

van den Bosch, R. C. E., van de Ven, G., Verolme, E. K., Cappellari, M., & de Zeeuw, P. T. 2008, MNRAS, 385, 647
van der Marel, R. P., Cretton, N., de Zeeuw, P. T., & Rix, H. 1998, ApJ, 493, 613
Van Wassenhove, S., Volonteri, M., Walker, M. G., & Gair, J. R. 2010, MNRAS, 408, 1139
Volonteri, M., & Perna, R. 2005, MNRAS, 358, 913
Walker, M. G., Mateo, M., & Olszewski, E. W. 2008, ApJ, 688, L75
Walker, M. G., Mateo, M., & Olszewski, E. W. 2009a, AJ, 137, 3100
Walker, M. G., Mateo, M., Olszewski, E. W., et al. 2006, AJ, 131, 2114
Walker, M. G., Mateo, M., Olszewski, E. W., et al. 2009b, ApJ, 704, 1274
Walker, M. G., & Peñarrubia, J. 2011, ApJ, 742, 20
Wolf, J., Martinez, G. D., Bullock, J. S., et al. 2010, MNRAS, 406, 1220
Wu, X. 2007, arXiv:astro-ph/0702233